Tidally driven interannual variation in extreme sea level frequencies in the Gulf of Maine

H. E. Baranes[1], J. D. Woodruff[1], S. A. Talke[2], R. E. Kopp[3], R. D. Ray[4], and R. M. DeConto[1]

[1]Department of Geosciences, University of Massachusetts Amherst, Amherst, MA, USA, [2]Civil and Environmental Engineering Department, California Polytechnic State University, San Luis Obispo, CA, USA, [3]Department of Earth & Planetary Sciences and Institute of Earth, Ocean & Atmospheric Sciences, Rutgers University, New Brunswick, NJ, USA, [4]Geodesy and Geophysics Laboratory, NASA Goddard Space Flight Center, Greenbelt, MD, USA

Corresponding author: Hannah Baranes (hbaranes@geo.umass.edu)

Key Points:

- We present a new quasi-nonstationary joint probability method that estimates tidally driven interannual fluctuations in flood hazard
- This method provides more precise and stable storm tide frequency estimates than extreme value distributions fit to measured storm tides
- In the Gulf of Maine, tides force decadal oscillations in the 1% annual chance storm tide at a rate exceeding mean historical sea-level rise

Abstract

Astronomical variations in tidal magnitude can strongly modulate the severity of coastal flooding on daily, monthly, and interannual timescales. Here, we present a new quasi-nonstationary skew surge joint probability method (qn-SSJPM) that estimates interannual fluctuations in flood hazard caused by the 18.6 and quasi 4.4-year modulations of tides. We demonstrate that qn-SSJPM-derived storm tide frequency estimates are more precise and stable compared with the standard practice of fitting an extreme value distribution to measured storm tides, which is often biased by the largest few events within the observational period. Applying the qn-SSJPM in the Gulf of Maine, we find significant tidal forcing of winter storm season flood hazard by the 18.6-year nodal cycle, whereas 4.4-year modulations and a secular trend in tides are small compared to interannual variation and long-term trends in sea-level. The nodal cycle forces decadal oscillations in the 1% annual chance storm tide at an average rate of ±13.5 mm/y in Eastport, ME; ±4.0 mm/y in Portland, ME; and ±5.9 mm/y in Boston, MA. Currently (in 2020), nodal forcing is counteracting the sea-level rise-induced increase in flood hazard; however, in 2025, the nodal cycle will reach a minimum and then begin to accelerate flood hazard increase as it moves toward its maximum phase over the subsequent decade. Along the world's meso-to-macrotidal coastlines, it is therefore critical to consider both sea-level rise and tidal non-stationarity in planning for the transition to chronic flooding that will be driven by sea-level rise in many regions over the next century.

Plain Language Summary

Coastal management practices around flood risk often rely on estimates of the percent chance of a particular flood height occurring within a year. For example, U.S. flood insurance requires designating areas with a 100-year flood recurrence interval (the "100-year flood zone"). When storms hit regions with large tides, the height and timing of high tide often determine flood severity. Thus, the relationship between flood height and annual frequency can be altered by natural, daily-to-decadal cyclical variation in tide heights. Here, we present a new method for calculating annually-varying flood height–frequency relationships based on known tidal cycles. Applying the new method in the Gulf of Maine, we find an 18.6-year-long tidal cycle (the *nodal cycle*) has forced decadal variation in the 1% annual chance flood at a faster rate than the historical average rate of sea-level rise over the past century. Currently, nodal cycle forcing is counteracting the sea-level rise-induced increase in flood hazard; however, in 2025, the nodal cycle will reach a minimum in the Gulf and then begin to accelerate flood hazard as it moves toward its maximum over the subsequent decade. It is therefore critical to consider sea-level rise and tidal variation in medium-term flood hazard planning.

Glossary of acronyms

GEV	Generalized Extreme Value distribution
GPD	Generalized Pareto distribution
GPD_{ST}	Generalized Pareto distribution fit to measured storm tides
JPM	Joint probability method
MSL	Mean sea level
NOAA	National Oceanic and Atmospheric Administration
qn-SSJPM	Quasi-nonstationary joint probability method
RJPM	Revised joint probability method
SLR	Sea-level rise
SSJPM	Skew surge joint probability method
$ST_{0.01}$	Storm tide at the 0.01 exceedances/year level

1 Introduction

Extreme coastal flooding poses a growing hazard to coastal communities (e.g. Hallegatte et al., 2013; Neumann et al., 2015). Management practices around flood risk often require estimates of extreme sea level recurrence intervals; for example, in the United States, federal flood insurance and building codes depend on estimates of the current 100-year flood zone (Galloway et al., 2006; Hunter, 2010; Buchanan et al., 2017). Coastal flood hazard, however, is not stationary. The relationship between flood height and recurrence interval is approximately log-linear, so even small interannual variations in storm surge, tides, waves, or mean sea-level (trends on the order of millimeters per year) can significantly alter extreme sea level frequencies (e.g. Oppenheimer et al., 2019). Robust statistical methods for considering sea-level non-stationarity (Hunter, 2010; Buchanan et al., 2017; Wahl et al., 2017) have been used to incorporate uncertain sea-level rise (SLR) projections into global (e.g. Lin et al., 2016; Garner et al., 2017; Oppenheimer et al., 2019) and local (e.g. NYC, 2013; Douglas et al., 2016; Griggs et al., 2017) hazard assessments. In this paper, we investigate the impact of quasi-deterministic variation in astronomical tides on low-frequency, high-impact extreme sea levels.

Tidal magnitude modulates the severity of flooding in meso-to-macrotidal regions, and interannual variation in tides causing periods of enhanced flood risk is a well-known phenomenon (e.g. Sobey, 2005; Eliot, 2010; Menéndez & Woodworth, 2010; Ray & Foster, 2016; Talke et al., 2018; Peng et al., 2019; Haigh et al., 2020; Talke & Jay, 2020). In particular, the 18.6-year lunar nodal cycle and the 8.85-year cycle of lunar perigee influence high water globally on weekly, monthly, and annual timescales (e.g., Haigh et al., 2011; Peng et al., 2019). Ray and Foster (2016) showed that the perigean cycle modulates predicted future nuisance tidal flooding at a quasi 4.4-year period. For extreme flooding, Menéndez and Woodworth (2010) modeled global nodal and perigean astronomical modulations using a non-stationary location parameter in extreme sea level probability distributions fit to satellite altimetry records over the 1970–2008 time period. Over a longer, nearly 200-year record from Boston, Massachusetts, Talke et al. (2018) also showed that the nodal cycle produces 10–20 cm of variation in extreme sea levels with recurrence intervals between 2 and 100 years.

On decadal to centennial timescales, non-astronomical factors also force local-to-global-scale variations and trends in tides (Schindelegger et al., 2018; Haigh et al., 2020; Talke & Jay, 2020). Changes in water depth, shoreline position, frictional resistance, and river flow have led to dramatic local-scale tidal amplification and reduction over the past two centuries, particularly in estuaries and tidal rivers (Winterwerp et al., 2013; Haigh et al., 2020; Talke & Jay, 2020).

Spatially coherent, regional-scale variation in tides has been driven by changes in ocean depth, shoreline position, sea ice extent, ocean stratification, non-linear interactions, and radiational forcing (e.g. Woodworth, 2010; Müller et al., 2011; Müller, 2012; Haigh et al., 2020).

In summary, interannual variations and long-term trends in tides have significant implications for flood hazard. Astronomical nodal and perigean cycles can significantly increase flood hazard compared to the long-term average during their positive phases (e.g. Talke et al., 2018), and secular changes in tides driven by non-astronomical factors will either enhance or counteract the increase in flood hazard driven by SLR (e.g. Haigh et al., 2020). Given that the expected frequency of flooding changes year-to-year, considering sea-level rise and tidal non-stationarity together is important to both short and long-term municipal planning and emergency management at the coast. However, as mentioned by Talke et al. (2018), methods for assessing tidally driven interannual variation in extreme sea-level hazard require further development.

In this paper, we describe a new method for estimating tidally driven non-stationarity in extreme still water levels measured at tide gauges using an adaptation of the measurement-based joint probability methods developed by Pugh and Vassie (1978, 1980), Tawn and Vassie (1989), Tawn (1992), and Batstone et al. (2013). We apply and validate our methodology using century-long tide gauge records from the Gulf of Maine coast in the northwest Atlantic Ocean (Fig. 1), a region with significant nodal variability and secular trends in tides (Ray, 2006; Ray & Talke, 2019). Under the assumption of stationary storm characteristics, this new quasi-nonstationary joint probability method provides separate statistical treatment of tides and surge and accounts for interannual variation in tides. We use the term "still water level" to convey that the tide gauge-based analyses presented here do not consider wave impacts. Tide gauges located in wave-sheltered harbors measure the contributions storm surge, tides, and mean sea level to flood level (i.e. the still water level) but exclude waves (Melet et al., 2018; Dodet et al., 2019; Woodworth et al., 2019). Note that in subsequent sections, we use the term "storm tides" for extreme still water levels referenced to the annual mean sea-level.

2 Background

2.1 Site description

We apply this new quasi-nonstationary joint probability method to estimating extreme still water level recurrence intervals at the three longest running and most complete National Oceanic and Atmospheric Administration (NOAA) tide gauge records within the Gulf of Maine at Boston, Portland, and Eastport (Fig. 1). Table 1 shows their locations, measurement timespans, and relevant tidal datums. An additional record at St. John, New Brunswick (1893-present) is not included because of significant data gaps and unusual interannual variation in the amplitude of the M_2 tidal constituent after 1980 (Ray & Talke, 2019). In addition to its multiple century-long tide gauge records, the Gulf of Maine's large tide range and known local and regional tidal variation make it an ideal location for applying our statistical method. The region also hosts major cities and sensitive infrastructure that require careful flood risk assessment; for example, Hallegate et al. (2013) ranked Boston, Massachusetts within the top twenty cities globally for modeled flood loss under both present-day and future (2050) scenarios.

The Gulf of Maine coast is vulnerable to flooding from both tropical and extratropical cyclones, but extratropical cyclones have historically been the dominant flooding mechanism, as they are more frequent and more likely to intersect with high tide due to their often longer durations (e.g. Kirshen et al., 2008; Talke et al., 2018). The total still water level (i.e. not

including waves) recorded during a storm, relative to some vertical datum, is called *storm tide* and represents the net impact of meteorological and tidal forcing. Here, we use annual mean sea level (MSL) as the vertical datum, such that storm tide time series do not include SLR. *Storm surge* is the meteorologically forced deviation from the predicted tide, calculated by subtracting the predicted tide from time series of measured storm tide values. Extreme storm surges reach ~1.3 meters in the Gulf (e.g. Talke et al., 2018), and tides are significantly larger. The great diurnal tide range increases northward from 3.1 meters in Boston to ~16 meters in the Bay of Fundy's northern embayments, making tides a primary control on most of the region's extreme coastal flooding events. In Boston, for example, Talke et al. (2018) found that 92 of the top 100 storm events occurring between 1825 and 2018 coincided with a predicted high tide that exceeded modern mean higher high water.

Tides in the Gulf of Maine and Bay of Fundy are unusual in several respects. In addition to the well-known large tidal range, there is a natural resonance frequency in the Gulf near the frequency of the N_2 tide (Garrett, 1972; Godin, 1993). Observed N_2 amplitudes are larger than S_2 amplitudes, although the opposite is true of the theoretical tidal potential; thus, the classic fortnightly spring-neap modulation is relatively weak and is smaller than the monthly modulation induced by M_2/N_2 beating. The strongest astronomical tides during any month therefore occur near times of lunar perigee. Similar to many locations, there are additional modulations at semiannual, 4.4-year, and 18.6-year periods (Haigh et al., 2011; Ray & Merrifield, 2019). The 4.4-year and 18.6-year modulations of the highest predicted tide are moderate at Boston and Portland (roughly 3–4 cm in amplitude) but get much larger (up to 15 cm in amplitude) inside the Bay of Fundy (Ray & Merrifield, 2019; see also Ray & Talke, 2019 for 18.6-year modulations of the M_2 constituent in the Gulf of Maine). The 18.6-year modulation is caused by the lunar nodal cycle, or a precession of the moon's orbital plane around the ecliptic 360° every 18.6 years. The 4.4-year modulation is caused by perigean spring tides coinciding with the winter or summer solstice (when the diurnal tidal contribution is largest) twice per 8.85 years (see Ray & Foster, 2016 for an explanation).

Perhaps owing to the basin resonance being near N_2, Gulf of Maine tides are sensitive to small changes in basin geometry, depth, and friction. Indeed, they display some of the largest secular tidal trends observed anywhere in the world for a regional body of water. Since the early-20^{th} century, the amplitude of the M_2 tidal constituent has steadily increased at an average rate of 0.25 ± 0.04 mm/y at the Boston tide gauge, 0.59 ± 0.04 mm/y at Portland, and 0.77 ± 0.08 mm/y at Eastport (Ray & Talke, 2019). In comparison, average rates of SLR measured at these tide gauges over the same time period (see Tab. 1 for exact date range) are 2.83 ± 0.15 mm/y in Boston, 1.88 ± 0.14 mm/y in Portland, and 2.14 ± 0.17 mm/y in Eastport. New tide estimates derived from 19^{th}-century water level measurements show that the M_2 trend began sometime in the late-19^{th} or early-20^{th} century, coincident with the transition to modern rates of SLR (Ray & Talke, 2019). Numerical models show that SLR has only caused part of the observed increase in M_2 amplitude in the Gulf of Maine (e.g. Müller et al., 2011; Greenberg et al., 2012; Pelling & Green, 2013; Schindelegger et al., 2018), suggesting that ocean stratification driven by sea-surface temperature warming has also played a role in the increase (Müller, 2012; Ray & Talke, 2019).

2.2 Review of extreme sea level statistical methods

Extreme sea level recurrence intervals can be estimated from data or models. In both cases, an extreme value probability distribution is fit to a set of measured or simulated extreme

sea levels assumed to be representative of the possible flood scenarios in a region. Hydrodynamic simulations have the advantage of explicitly including wave impacts and providing spatially continuous flood elevations and flow velocities; however, they are computationally intensive, take time to develop, and as with all models, rely on uncertain parameterizations, bathymetry, and assumptions (e.g. Vousdoukas et al., 2016; Lin et al., 2010). At gauged locations with multi-decadal records, estimating storm tide recurrence intervals from data is a simpler alternative that will be the focus of this paper.

The two most commonly used extreme value distributions are the Generalized Extreme Value distribution (GEV) and the Generalized Pareto Distribution (GPD). The GEV is fit to block maxima data, or the n-largest measurements per some time interval (e.g. the largest event each year), and the GPD is fit to peaks-over-threshold data, or all measurements over some threshold value that defines extremes. The GPD approach is more robust because it uses more available extreme observations (e.g. NERC, 1975; Coles et al., 2001; Tebaldi et al., 2012; Buchanan et al., 2017). In Boston, for example, only 46 of the top 100 storm tides recorded at the NOAA gauge occurred in distinct years. A GEV using annual block maxima would therefore omit more than half of the top-100 events. Compared with the GEV, however, the GPD requires higher data quality and is more difficult to fit automatically because of its sensitivity to the choice of threshold (Coles, 2001; Arns et al., 2013). Storm tide statistics published by NOAA, for example, are derived from GEV fits because choosing a GPD threshold can be subjective, and NOAA requires a method that can be quickly applied and periodically updated at over 100 gauges (Zervas, 2013). Nonetheless, Talke et al. (2018) found that GEV and GPD fits to Boston extreme storm tides yielded similar recurrence interval estimates.

In meso-to-macrotidal regions, where tides are a primary control on flooding, a joint probability approach that convolves separate tide and surge distributions can capture more extreme storm surges within a temporally limited tide gauge record (e.g. Pugh & Vassie, 1979, 1980). For example, in 63 of the 100 years in Boston's record, the largest storm surge of the year did not coincide with any of the year's top-3 storm tides; thus, a GPD fit to measured Boston storm tides would exclude two-thirds of the largest storm surges (assuming a GPD threshold that was exceeded, on average, three or fewer times per year). The first two published storm tide joint probability methods were the Joint Probability Method (JPM; Pugh & Vassie, 1978, 1980) and the Revised Joint Probability Method (RJPM; Tawn & Vassie, 1989; Tawn, 1992). The JPM separates measured water levels into the predicted tide and a non-tidal residual (measured minus predicted water level at a given time), fits an empirical probability distribution to each component, and obtains the joint storm tide distribution by a convolution of the two component distributions. The RJPM improves upon the JPM by 1) fitting a GEV distribution to extreme non-tidal residual values in order to model events exceeding the observed maximum, and 2) applying an extremal index that accounts for dependence of non-tidal residuals occurring close together in time (the extremal index will be further explained in section 3.2).

The primary shortcoming of the JPM and RJPM is the assumed independence between the predicted tide and the non-tidal residual. Storm surge and tides interact; storm surge increases water depth, and tidal wave speed increases in deeper water (Horsburgh and Wilson, 2007). The non-tidal residual time series of measured minus predicted water level therefore often includes an "illusory" surge during storm events, which is an artifact of the difference in the predicted tide and the phase-shifted tide. Furthermore, the amplitude, timing, and timescale of the surge wave impacts its frictional interaction with tides (Familkhalili et al., 2020).

The Skew Surge Joint Probability Method (SSJPM; Batstone et al., 2013) improves upon the JPM by eliminating the bias introduced by the uncertain timing of the tidal prediction during storm conditions. *Skew surge* is defined as the difference between the maximum measured water level and the predicted high water within each tidal cycle. After accounting for seasonal variation in tides, Williams et al. (2016) found statistical independence between predicted high water and skew surge at 77 Atlantic tide gauges in the United States and Europe. They concluded that this skew surge independence enables a simplified joint probability approach for calculating storm tide recurrence intervals that does not require the inclusion of an empirical relationship between tide and the non-tidal residual to account for tide-surge interaction. The argument is primarily statistical and not dynamical, as the absence of correlation does not indicate the absence of effect; rather, in observational records, natural variability in storm systems dominates over tidally driven variation in surge. We address this issue by using primarily coastal (rather than estuary) locations, such that frictional interaction effects are likely less prominent.

These joint probability methods have lowered bias in storm tide recurrence interval estimates (compared to GPD or GEV fits to data) in regions where tides are large relative to meteorological forcing, particularly for short data series (Dixon & Tawn, 1999; Haigh et al., 2010); however, none has accounted for year-to-year fluctuations or secular trends in tidal properties. In the following sections, we describe a new, quasi-nonstationary (*qn*) modification of the SSJPM called the *qn-SSJPM*, which calculates a separate set of storm tide recurrence intervals for winter and summer storm seasons using that season's known high tides. We fit separate summer and winter distributions because the region's large storm events mostly occur in the winter season (e.g. Talke et al., 2018), while summertime tide levels are larger on average (Ray & Foster, 2016).

3 Methods

3.1 Tide gauge data processing

At the Eastport, Portland, and Boston NOAA gauges, we use hourly water level data from NOAA, downloaded from the University of Hawaii Sea Level Center database for pre-2016 data (Caldwell et al., 2010) and from NOAA's website for post-2016 data (https://tidesandcurrents.noaa.gov). We remove the annual MSL trend by subtracting a one-year moving average of all hourly water level measurements (following Arns et al., 2013).

We fit a six-minute cubic spline function to the hourly data over the entire length of each tide gauge record (six-minute data are only available from NOAA beginning in 1996) to reduce the peak truncation caused by using hourly records. For example, hourly-based high waters from Boston in 2018 were an average of 4.1 cm lower than 6-minute resolution records. The six-minute spline fit reduces this bias to 0.7 cm. Since the precision of individual, pre-digital measurements varies from 0.015 meters (due to rounding) to 0.05–0.1 meters or more during periods with timing or gauge problems (e.g. Talke et al., 2018, 2020), this small bias is less than other sources of error. All subsequent calculations use this MSL-adjusted six-minute spline fit to the hourly data.

We estimate the tidal contribution to each water level measurement using the MATLAB-based harmonic analysis program r_t_tide (Pawlowicz et al., 2002; Leffler and Jay, 2009). We calculate tidal constituents independently for each year from a 369-day analysis that includes 67 constituents. The 369-day analysis enables estimation of the semiannual and annual constituents, as well as the seasonal sidelines to M_2 (often called MA_2 and MB_2, but mislabeled H_1 and H_2 in

r_t_tide). Since we are interested in the effect of the nodal cycle, no nodal corrections were applied. r_t_tide also applies nodal corrections based on the astronomic potential, rather than the empirically measured and slightly smaller correction observed in practice in the Gulf of Maine (e.g. Ku et al., 1985; Ray & Foster 2016; Ray & Talke, 2019).

We calculate the skew surge parameter by subtracting maximum predicted water level from maximum observed water level within each semidiurnal tidal cycle. Following Williams et al. (2016), we test for statistical independence between predicted high water and the top 1% of skew surge at all sites using the rank-based Kendall's Tau correlation test (Kendall, 1938), where the criteria for significant correlation are $|tau| > 0.1$ and $p < 0.05$. We do not find significant correlation between predicted high water and skew surge at any of the three sites (Tab. S1).

The final inputs into the joint probability analysis are semidiurnal predicted high waters (relative to annual MSL) and their associated skew surges over the length of each tide gauge record. Measured high waters are only used to calculate the declustering coefficient (see equation 6 for calculating the extremal index in section 3.2). Prior to the joint probability analysis, we also divide tides and skew surges into the winter storm season, defined as 31 October to 30 April, and the more quiescent summer season, defined as 1 May to 30 October (Wahl and Chambers, 2015; Thompson et al., 2013). Including 31 October in the winter storm season avoids exclusion of a 1991 hybrid storm (Talke et al., 2018). In all subsequent analyses, we only include seasons where the set of measured water levels is at least 75% complete (Menéndez and Woodworth, 2010; Wahl and Chambers, 2015). Table 1 lists the winter and summer seasons omitted at each tide gauge.

3.2 Quasi-nonstationary joint probability analysis (qn-SSJPM)

We calculate storm tide exceedance curves for each season, where the expected number of exceedances (i.e. the number of storm tides exceeding a certain level) is equal to the inverse of recurrence interval. Each winter or summer-season storm tide exceedance curve is calculated by convolving probability distributions of that season's predicted high waters and all winter or summer skew surges recorded over the length of the tide gauge record. We model winter and summer extreme skew surge probabilities with a GPD following Batstone et al. (2013). For skew surges x above a threshold μ, the GPD cumulative distribution function $G_{ss}(x)$ takes the form

$$G_{ss}(x) = 1 - \left(1 + \xi \frac{x-\mu}{\sigma}\right)^{-1/\xi} \quad (1)$$

with shape parameter $\xi \neq 0$ and scale parameter $\sigma > 0$. To account for uncertainty in the skew surge GPD, we sample 1,000 pairs of ξ and σ from the covariance matrix of their maximum likelihood estimates with Latin hypercube sampling (Buchanan et al., 2016, 2017). We choose the GPD threshold that defines extreme skew surges by minimizing the root mean square error of GPD exceedances versus empirically-derived storm tide plotting positions (Arns et al., 2013). We calculate plotting positions using the Weibull formula

$$\tilde{F}_{ss}(x_i) = \frac{i}{n+1} \quad (2)$$

where x_i is the ith-largest skews surge, and n is the total number of skew surges. We find that setting the threshold as the 99.7th percentile of skew surges for both the winter and summer seasons minimizes error across all sites, and past studies have used a similarly high threshold (Menéndez and Woodworth, 2010; Arns et al., 2013). This 99.7th percentile threshold samples an average of 1.1 events per season. Following Batstone et al. (2013), we assume there are

sufficient observations to use the empirical distribution $\tilde{F}_{ss}(x)$ (i.e. plotting positions; equation 2) for skew surges below the threshold, such that the cumulative distribution function of all skew surges $F_{ss}(x)$ is

$$F_{ss}(x) = \begin{cases} \tilde{F}_{ss}(x), & x < \mu \\ (1 - 0.997) * G_{ss}(x) + 0.997, & x \geq \mu \end{cases} \quad (3)$$

We then calculate the joint cumulative distribution function of storm tides $F_{ST}(z)$ for each season following the SSJPM (Batstone et al., 2013), which assumes that there is an equal probability of a given skew surge occurring at any high tide in a season:

$$F_{ST}(z) = \left[\prod_{t=1}^{N_{HW}} F_{ss}(z - P_t)\right]^{1/N_{HW}} \quad (4)$$

where z is storm tide, P_t is the predicted high water in tidal cycle t, and N_{HW} is the total number of high waters in the season. To account for statistical uncertainty in the skew surge GPD parameters, tides are convolved with all 1,000 skew surge GPDs (F_{ss}). The 50th quantile of the resulting 1,000 storm tide distributions (F_{ST}) represents the central estimate, and the 5th and 95th quantiles provide a 90% uncertainty range. We convert storm tide cumulative probabilities to expected number of exceedances per season *N(z)* by

$$N(z) = [N_{HW} * \theta(z)] * [1 - F_{ST}(z)] \quad (5)$$

where $\theta(z)$ is the extremal index, which effectively reduces the number of high waters per season to the number of independent high waters per season to account for events that span multiple high tides (Leadbetter, 1983; Tawn, 1992). The extremal index is the inverse of mean cluster size (the mean number of storm tides exceeding a certain height that are associated with a single event) and calculated as a function of storm tide, following Ferro and Segers (2003):

$$\frac{1}{\theta(z)} = \frac{2\left[\sum_{i=1}^{E(z)-1}(I(z)_i - 1)\right]^2}{(E(z) - 1) * \sum_{i}^{E(z)-1}[(I(z)_i - 1) * (I(z)_i - 2)]} \quad (6)$$

where *E(z)* is the number of measured storm tides exceeding *z*, and *I(z)* is interexceedance time. We find that the extremal index reduces storm tide magnitudes in the 1 to 30-year recurrence interval range; thus, it is likely that these water levels are sometimes exceeded multiple times during a single storm event, while the most extreme water levels with recurrence intervals longer than 30 years are generally independent.

At each site, the final products of the qn-SSJPM calculations include:

1. A storm tide exceedance curve for each summer and winter season in the NOAA record
2. Full-year (i.e. combined winter and summer) storm tide exceedance curves for each year in the NOAA record, calculated by adding the expected number of summer and winter exceedances in a given year for each storm tide height
3. Two time-averaged storm tide exceedance curves (one winter, one summer), calculated using winter or summer tides over the full length of the NOAA record
4. One full-year, time-averaged storm tide exceedance curve

4 Results and discussion

4.1 qn-SSJPM results

We focus our discussion on winter storm season results because extreme flooding is primarily a winter hazard in the Gulf of Maine. A comparison of the time-averaged qn-SSJPM storm tide exceedance curves for winter, summer, and the full year (Fig. 2a) shows that storm tides from the full-year curves are, at most, 1.5 cm higher than winter curves at frequencies below 0.1 expected exceedances/year. Thus, when viewing the full-year curve, it is important to do so with the caveat that summer floods are only a minor contributor to total flood hazard.

Figure 2b shows the winter-season annual and time-averaged storm tide exceedance curves for Eastport, Portland, and Boston. The spread among annual curves represents deterministic tidal variability and is thus greatest in Eastport where tide range and nodal cycle amplitude are the largest. As an example, the winter storm tide with 0.01 expected exceedances/year ranges 4.20–4.50 meters in Eastport, 2.56–2.74 meters in Portland, and 2.83–2.99 meters in Boston depending on the tidal properties of the calendar year (note that all storm tides are relative to annual MSL). The 90% uncertainty region (blue shading in Fig. 2b) encompasses both deterministic tidal variability and statistical uncertainty in the skew surge GPD parameters.

We also compare qn-SSJPM storm tide exceedance distributions to a GPD fit to the top 0.3% of storm tides in each record (Fig. 2b). This is a common approach for deriving storm tide exceedances (see section 2.2), hereafter referred to as GPD_{ST}. We fit GPD_{ST} following the same methods described in section 3.2 for fitting the skew surge GPD, using the 99.7^{th} percentile of measured storm tides as the GPD threshold. Uncertainty ranges are larger for the GPD_{ST} distributions than the qn-SSJPM distributions (gray versus blue shaded regions in Fig. 2b). Although both incorporate GPD parameter uncertainty, for the qn-SSJPM, the deterministic predicted high water distribution reduces overall uncertainty. In Boston, the GPD_{ST} method estimates significantly higher winter storm tides at exceedance levels < 0.1 compared to the qn-SSJPM. Given the disagreement, we 1) use Monte Carlo simulations to validate the two statistical approaches, 2) compare the Boston qn-SSJPM and GPD_{ST} exceedance curves to a GPD_{ST} exceedance curve fit to an extended, 200-year long record of Boston storm tides (Talke et al., 2018), and 3) test for sensitivity to GPD threshold selection for in each method.

4.2 Monte Carlo validation

We compare the validity of the qn-SSJPM and GPD_{ST} methods using Monte Carlo simulations. We create a synthetic 10,000-year time series of winter-season high waters by splicing together the 1921-2018 Boston winter-season predicted high waters 102 times (102 times the 98-year record ≈ 10,000 years) and combining each predicted high water with a skew surge randomly sampled from the cumulative distribution function of Boston winter skew surges. We treat empirical storm tide exceedances calculated from the synthetic 10,000-year record (equation 2) as the "truth." We then run 1,000 trials of randomly selecting 100 of the 10,000 years and calculating storm tide exceedance distributions based on those 100 years using both the qn-SSJPM and GPD_{ST} methods. We use the 99.7^{th} percentile storm tide and skew surge as GPD thresholds, and for the qn-SSJPM calculation, we only generate a single time-averaged storm tide exceedance distribution for the 100 years (i.e. we do not calculate annual distributions). These simulations test how reliably the two statistical methods can represent flooding conditions over 10,000 years based on a limited "observational" period of 100 years.

In analyzing the results, "estimate" refers to the storm tide-exceedance relationship calculated from a 100-year subsample using the qn-SSJPM or GPD_{ST} methods. "Truth" refers to the empirical storm tide-exceedance relationship calculated from the synthetic 10,000-year record. For each of the 1,000 trials, we determine 1) whether or not the truth falls within the central 67% ranges of storm tide estimates at the 0.1, 0.01, and 0.002 exceedances/year levels for the two methods, and 2) the bias of the estimates, calculated as the difference between the truth and the central (50^{th} quantile) qn-SSJPM and GPD_{ST} storm tide estimates at the 0.1, 0.01, and 0.002 exceedances/year levels.

We find that the truth falls within the central 67% range of estimates 55–65% of the time for the qn-SSJPM and 59–67% of the time for GPD_{ST} (Fig. 3a). Both methods' overlap with the truth generally increases at lower exceedance levels because uncertainty range also increases with decreasing expected exceedances. The lower coverage of qn-SSJPM error ranges indicates that the method's estimate errors are more overconfident than GPD_{ST} estimate errors; however, both the qn-SSJPM and GPD_{ST} have reasonable coverage.

Comparing biases in qn-SSJPM and GPD_{ST} estimates of storm tides at the 0.1, 0.01, and 0.002 exceedances/year levels reveals that qn-SSJPM estimates are more precise and stable (i.e. consistently closer to the truth). Box plots in Figure 3b show each method's biases for all 1,000 trials. The interquartile ranges increasing (i.e. the boxes getting larger) at lower exceedance levels reflects the expected trend of increasing instability (i.e. variability) in estimated exceedances at lower exceedance levels for a given record length (e.g. Haigh et al., 2010). Mean bias is close to zero for both methods at all three exceedance levels; however, for storm tides at the 0.01 and 0.002 exceedances/year levels, both the interquartile range and total range in biases are significantly narrower for qn-SSJPM estimates than for GPD_{ST} estimates. This result indicates that for a 100-year observational record, both methods will, on average, provide accurate storm tide estimates between the 0.1 and 0.002 exceedances/year levels; however, GPD_{ST} estimates of storm tides with recurrence intervals nearing the record length (e.g. the storm tide with a 100-year recurrence interval or 0.01 expected exceedances/year for a 100-year-long record), are more susceptible to being biased by the largest few events within the observational period. This finding is consistent with past studies that have shown GPD and GEV fits to observed storm tides (often called "direct methods" of estimation) are more unstable to historical outlier events than joint probability distributions that incorporate large historical storm surges not necessarily coinciding with high tides (e.g. Tawn and Vassie, 1989; Tawn, 1992; Haigh et al., 2010).

This instability to historical outliers partially explains the disagreement between the qn-SSJPM and GPD_{ST} curves for Boston (Fig. 2b). Boston's highest three recorded flood events all occurred in years with unusually large tides (Talke et al., 2018). For example, the Blizzard of 1978 (the storm tide of record), happened to coincide with the year that, on average, had the largest-magnitude high waters over the past century (represented by the right-most blue curve in Fig. 2b and highlighted with a red arrow in Fig. 5). Thus, the GPD_{ST} method in part overestimates Boston flood hazard because it does not account the Blizzard of 1978's 3.05-meter flood having had a lower probability of occurrence during any of the other 97 winters of record.

4.3 Extended Boston record and GPD threshold sensitivity

Comparing the Boston qn-SSJPM and GPD_{ST} winter storm tide exceedance curves (Fig. 2b) to exceedance curves fit to the Talke et al. (2018) extended 200-year storm tide record also highlights the stability of the qn-SSJPM relative to the GPD_{ST} method. Gray curves in Figure 4

show five GPD_{ST} fits to the 1921–2018 NOAA record using five different GPD thresholds, ranging 2.25 to 2.44 meters (the 99.5th to 99.9th percentiles of measured winter storm tides; Tab. S2). For the 100-year NOAA record, the five exceedance curves begin to diverge below the 0.03 exceedances/year level, demonstrating the sensitivity of the GPD_{ST} method to threshold selection. The red shaded region in Figure 4 shows GPD_{ST} curves fit to the extended 1825–2018 Boston record (un-bias corrected Data Set S3 from Talke et al., 2018) using both a 2.40-meter threshold (the value used by Talke et al., 2018) and a 2.31-meter threshold (the value used in Fig. 2b that provides the best match to empirical exceedances). In contrast to the NOAA-record curves, the narrowness of the red shaded region indicates that the longer, 200-year dataset makes the GPD_{ST} method stable down through the 0.002 exceedances/year level.

The blue shaded region in Figure 4 shows the qn-SSJPM fit to the NOAA record using five different thresholds for the GPD fit to skew surges (99.5th through 99.9th percentiles; Tab. S2). The small variability among the five curves (i.e. the narrowness of the blue shaded region) shows that with the shorter NOAA record, the qn-SSJPM can achieve the same stability with respect to GPD threshold selection as the GPD_{ST} fit to the 200-year record. Finally, the agreement at low exceedance levels between the qn-SSJPM and 200-year exceedance curves is further evidence that the qn-SSJPM provides a more reliable characterization of extreme storm tide frequencies than the GPD_{ST} method based on the 100-year NOAA record.

4.4 Interannual variation in storm tide frequency

Interannual variation in tides forces changes in flood hazard on annual-to-decadal timescales that should be considered in coastal management practices tied to storm tide frequency estimates. We quantify the tidal modulation of flood hazard over the past century in Eastport, Portland, and Boston using the annual time series of winter storm season storm tides at the 0.01 exceedances/year level (hereafter referred to as $ST_{0.01}$) taken from the qn-SSJPM curves (Fig. 5). To represent the three dominant sources of interannual tidal variability in the region (see Ray & Foster, 2016), we fit a harmonic function to the time series with an 18.6-year period, a 4.4-year period, and a linear trend, where $ST_{0.01}$ values are relative to annual MSL, so the linear trend is the increase in tides above SLR. The ranges (twice the amplitudes) of the 18.6 and 4.4-year harmonics represent the magnitudes of the tidal cycles' forcing of flood hazard.

Table 2 compares 18.6 and 4.4-year modulations of $ST_{0.01}$ and of the highest predicted tide (the highest tide in a 6-month interval), which are computed directly from harmonic constants at the gauges. The 18.6 and 4.4-year cycles' forcing of $ST_{0.01}$ is perhaps smaller than that of the highest predicted tide because $ST_{0.01}$ is calculated from observations rather than predictions. Observed water level data include atmospheric effects, which introduce variability that could interfere with tidal modulations. The exclusion of summer-season tides in the winter $ST_{0.01}$ values also likely reduces 4.4-year periodicity in predicted water levels (e.g. Talke et al., 2018). Finally, Peng et al. (2019) showed that the 18.6-year modulation of tides is greater for more extreme high waters (for example, the modulation of monthly maximum high waters is greater than that of monthly 99^{the} percentile high waters). Similarly, modulation of $ST_{0.01}$ potentially reflects less extreme tidal levels than what would be obtained using the 6-month maximum.

The secular increase in tides observed in the M_2 tidal constituent (e.g. Ray & Talke, 2019) has driven roughly a 0.6 mm/y increase in $ST_{0.01}$ in Eastport and Portland. In Boston, however, there is a slight negative linear trend in $ST_{0.01}$ of -0.08 mm/y. Thus, the increase in tides has had a minimal decadal-timescale impact on $ST_{0.01}$ compared to other forcings; however, in

Eastport and Portland, the total secular increase in $ST_{0.01}$ over the length of the tide gauge record is comparable to decadal nodal variability. There is likely to be a future increase in high water levels with SLR (Greenburg et al., 2012; Pelling & Green, 2013; Schindelegger et al., 2018) and increasing tidal range (Greenberg et al., 2012), but there are no detailed projections for Gulf of Maine tides that consider additional forcing mechanisms, such as changes in stratification and flooding (Haigh et al., 2020).

The significance of the 4.4 and 18.6-year tidal modulations of $ST_{0.01}$ can best be illustrated by converting the tidal cycle forcing ranges to rates and comparing them to rates of SLR. In Eastport, for example, the average range in 18.6-year forcing of $ST_{0.01}$ is 126 mm (Fig. 5). The 18.6-year forcing can be positive or negative, so over any half nodal period in Eastport, the average rate of nodal forcing of $ST_{0.01}$ is ±126 mm per 9.3 years, or ±13.5 mm/year. Applying the same calculation to Portland and Boston, the average 18.6-year tidal forcing rates are ±4.0 mm/year and ±5.9 mm/year, respectively. 4.4-year tidal forcing rates are a slower ±3.0 mm/year in Eastport and Boston and ±4.0 mm/year in Portland. In practice, however, interannual variation in winter MSL (which has historically been on the order of tens of mm) would drown out this shorter-period 4.4-year tidal modulation.

Figure 6 provides a visualization of the impact of 18.6-year forcing in the context of SLR. On decadal timescales, the natural variability in $ST_{0.01}$ (and therefore flood hazard) driven by the nodal cycle at the three Gulf of Maine sites has historically been larger than non-stationarity driven by the ~100-year average rate of SLR (black triangles versus asterisks in Fig. 6). In the future, even as SLR accelerates to equal or exceed rates of $ST_{0.01}$ nodal forcing, the nodal cycle will continue to force significant decadal-scale variability in the rate that flood hazard will increase. We illustrate this effect through 2100 by adding the $ST_{0.01}$ nodal forcing rate to the projected mean rate of SLR over 9.3-year periods when nodal forcing will be trending positively (i.e. moving from a minimum toward a maximum). Over 9.3-year periods when the nodal cycle will be trending negatively, we subtract nodal forcing from projected SLR. We use Kopp et al. (2014) probabilistic local SLR projections, but we modify the ice sheet contributions by replacing the Church et al. (2013) likely ranges with Oppenheimer et al. (2019) likely ranges.

The nodal cycle is currently in its negative phase in the Gulf, and until it reaches its minimum in 2025, negative nodal forcing will counteract the SLR-induced increase in flood hazard. Between 2025 and 2034 (and in all decades when the nodal cycle is moving from a minimum to a maximum), however, positive nodal forcing will accelerate the flood hazard increase. Thus, it is critical to consider SLR and nodal cycle forcing together in planning for the transition to chronic flooding that will be driven by SLR in many coastal regions over the next century (e.g. Ray & Foster, 2016; Buchanan et al., 2017; Kopp et al., 2017; Talke et al., 2018; Oppenheimer et al., 2019).

4.5 Limitations

We demonstrate that the qn-SSJPM provides more precise and stable storm tide exceedance estimates than the commonly used GPD fit to measured storm tides. However, there are sources of uncertainty in the method, and there are additional forcings of interannual storm tide variation that we do not account for. The skew surge GPD is a significant source of uncertainty, as GPD parameters are sensitive to both the choice of threshold (e.g. Coles, 2001; Arns et al., 2013) and the largest observed skew surge values (e.g. Tawn and Vassie, 1989; Tawn, 1992; Haigh et al., 2010). We show that the qn-SSJPM is stable against a range of skew surge GPD thresholds for Boston through the 0.002 exceedances/year level (Fig. 4), and this

should always be tested. Furthermore, the accuracy of skew surge values depends on the accuracy of tidal predictions. The r_t_tide software does not include minor constituents (for example, our Boston r_t_tide predictions use 67 constituents, compared to the 108 used by Ray and Foster, 2016), and our calculations do not include tide prediction errors. The errors, however, are small; for example, M_2 amplitude errors are on the order of 0.1% (~0.001–0.003 meters).

The qn-SSJPM also does not incorporate climatic variability that may impact storm tide hazard relative to annual MSL. For example, the North Atlantic Oscillation drives interannual variation in New England sea levels via northeasterly wind stress anomalies on the upper ocean (Goddard et al., 2015). In the future, increasing sea surface temperatures and changing atmospheric circulation patterns may also drive changes in storm intensity and frequency, but there is low confidence in site-specific projections of future storm behavior (e.g. Knutson et al., 2010; Emanuel et al., 2013), making it difficult to incorporate storm non-stationarity into flood hazard assessment.

Finally, the qn-SSJPM does not consider the impact of wave processes on flood hazard and is therefore most suitable for wave-sheltered harbors and embayments. During flood events, wave set-up elevates the time-averaged water level, and wave run-up periodically further raises water level (Stockdon et al., 2006; O'Grady et al., 2019). These processes must be included for hazard analyses to be reliable at wave-exposed coastlines; for example, Lambert et al. (2020) demonstrate that neglecting waves can lead to overestimating the time it will take for sea-level rise to double the frequency of a given extreme water level. Furthermore, our analysis does not explicitly account for water level oscillations just below wind-wave frequencies in the infragravity spectrum, generally defined between 0.04 and 0.004 Hz (Bertin et al., 2018). Infragravity waves are not only an important component of wave-induced run-up along open coasts (Stockdon et al., 2006), but can also contribute to flooding in harbors, particularly when amplified by resonance (e.g. Rabinovich, 2010; Bertin et al., 2015).

5 Conclusions

We present a new quasi-nonstationary skew surge joint probability method for calculating storm tide exceedances and apply it along the Gulf of Maine coast, where tides are large and vary year-to-year. In addition to providing separate statistical treatment of tides and surge, the qn-SSJPM calculates distinct annual storm tide exceedance curves that account for interannual variation in tides. Each year's curve is a convolution of 1) predicted high water probabilities, which are known based on that year's tide predictions, and 2) skew surge probabilities determined from a GPD fit to all skew surges recorded over the length of a tide gauge record.

We use a Monte Carlo validation and a GPD threshold sensitivity test to compare the qn-SSJPM to the commonly used method of fitting a GPD to times series of measured storm tides. We find that the qn-SSJPM provides more precise and stable storm tide frequency estimates because it is less susceptible to being biased by the largest few events within the observational period, and it is more stable with respect to GPD threshold selection. We also show that in Boston, qn-SSJPM-derived storm tide frequency estimates based on the 100-year NOAA record match those based on the extended, 200-year Talke et al. (2018) record.

At all three Gulf of Maine sites, we find that interannual variation in tides significantly impacts design-relevant flood levels, such as winter storm tides at the 0.01 exceedances/year level ($ST_{0.01}$). The 18.6-year nodal cycle forces decadal oscillations in $ST_{0.01}$ at a rate of 13.5

mm/year in Eastport, 4.0 mm/year in Portland, and 5.9 mm/year in Boston. In comparison, the average historical rate of local SLR over the past century has been between 1.89 and 2.86 mm/year at the three sites. Nodal forcing is currently counteracting the SLR-induced increase in flood hazard; however, in 2025, the nodal cycle will reach a minimum and then begin accelerating flood hazard increase as it moves toward its maximum phase over the subsequent decade.

SLR is driving a transition to severe chronic flooding in many coastal regions (e.g. Oppenheimer et al., 2019). Flooding becomes severe when water elevations cross thresholds defined by local topography and flood defense structures, and the nodal cycle entering a positive phase may drive flood heights above these thresholds sooner than SLR would alone. Thus, considering tidal non-stationarity and SLR together is key to long-term municipal planning and emergency management along meso-to-macrotidal coastlines.

Acknowledgments and Data

H.E.B. was supported by the National Aeronautics and Space Administration (Award NNX16AO24H). We thank two anonymous reviewers whose comments improved the manuscript. Datasets for this research are available in these in-text citation references: Caldwell et al. (2010), Talke et al. (2018), and https://tidesandcurrents.noaa.gov. All of the code we used to produce results is available at https://doi.org/10.5281/zenodo.3898657 with a Creative Commons Attribution 4.0 International license.

584 **Table 1.** Gulf of Maine NOAA tide gauge station info. The two right-most columns show winter
585 and summer seasons omitted from the qn-SSJPM statistical analysis due to missing more than
586 25% of water level measurements. Two years are listed for each omitted winter season because
587 we define the season as 31 October through 30 April of the following year. Note that all records
588 extend to the present, but we only use data through 2019 in our calculations.

Station; NOAA station no.	Approx. location	Mean higher high water (m)[a]	Great diurnal range (m)[a]	Timespan	Omitted winter seasons (< 75% complete)	Omitted summer seasons (< 75% complete)
Eastport, ME; 8410140	44°54.2'N 66°59.1'W	2.916	5.874	1929–2019	1957/1958, 1962/1963, 1970/1971, 1971/1972, 1974/1975, 1975/1976, 1976/1977, 1977/1978, 1995/1996, 1998/1999	1929, 1957, 1958, 1963, 1971, 1974, 1976, 1978, 1980
Portland, ME; 8418150	43°39.3'N 70°14.8'W	1.513	3.019	1910–2019	1910/1911, 1911/1912, 1933/1934, 1945/1946, 1960/1961	1910, 1911, 1956, 1961, 1970, 1971, 1990
Boston, MA; 8443970	42°21.2'N 71°3.0'W	1.545	3.131	1921–2019	1944/1945	1921

589 [a] Tidal datums are relative to 1983-2001 mean sea level
590

591 **Table 2.** Ranges of 18.6 and 4.4-year tidal cycle modulations of the storm tides at the 0.01
592 exceedances/year level ($ST_{0.01}$) and the highest predicted tide.

	18.6-year modulation range (mm)		Quasi 4.4-year modulation range (mm)	
	$ST_{0.01}$	Highest predicted tide	$ST_{0.01}$	Highest predicted tide
Eastport	126	196	28	78
Portland	37	66	37	68
Boston	55	72	28	62

593
594

595 **Figure 1.** Gulf of Maine site map, including gauge locations mentioned in the text.

596

597 **Figure 2.** Gulf of Maine storm tide exceedance curves. *(a)* Seasonality of flood hazard.
598 Historical time-averaged qn-SSJPM storm tide exceedance curves are compared for the full year
599 (thick solid line), summer season (dashed line), and winter season (thin solid line). *(b)*
600 Comparison of winter-season storm tide exceedance curves for the qn-SSJPM and a GPD fit to
601 measured storm tides (GPD_{ST}). Thin blue curves show qn-SSJPM-derived curves for each winter
602 storm season in the tide gauge record, and bold blue curves are the time-averaged qn-SSJPM
603 curves based on the entire tide gauge record. Black curves are a GPD_{ST} fit to the top 0.3% of
604 storm tides in each tide gauge record, and + signs are empirical exceedances (see equation 2).
605 Lines represent central estimates (50^{th} quantile), and filled regions show the 90% uncertainty
606 range (5^{th}–95^{th} quantiles) for each method.

Figure 3. Validation results. *(a)* Percent of the 1,000 validation trials that contain the truth (empirical value) within the central 67% range of storm tide estimates at the 0.1, 0.01, and 0.002 exceedances/year levels for the qn-SSJPM method (blue) and the GPD_{ST} method (gray). *(b)* Box plot showing the distribution of qn-SSJPM and GPD_{ST} biases for the 1,000 validation trials at the 0.1, 0.01, and 0.002 exceedances/year levels. Biases are calculated as the difference between the truth (based on the empirical distribution calculated from the 10,000-year synthetic record) and the central qn-SSJPM estimates (blue) or GPD_{ST} estimates (gray). Central marker is the median (with the * symbol showing the mean), and bottom and top box edges are the 25^{th} and 75^{th} quartiles. Values plotted as outliers (+ markers) fall outside the central 99.3% range.

Figure 4. Sensitivity of Boston winter storm tide exceedance curves to GPD threshold selection and comparison to the extended, 200-year Talke et al. (2018) record. The five gray storm tide exceedance curves are calculated using a GPD fit to measure storm tides in the 100-year NOAA record (GPD_{ST} method) with the threshold set as the 99.5^{th}, 99.6^{th}, 99.7^{th}, 99.8^{th}, and 99.9^{th} percentile of measured storm tides. The red shaded region shows GPD_{ST} exceedance curves fit to the 200-year Talke et al. (2018) record using a 2.31-meter threshold (same as Fig. 2b) and a 2.4-meter threshold (value used by Talke et al.). The blue shaded region shows five qn-SSJPM exceedance curves fit to the 100-year NOAA record, with the skew surge GPD threshold set as the same five percentiles of skew surges (99.5^{th}–99.9^{th} percentiles).

Figure 5. Interannual variation in the winter storm tides at the 0.01 exceedances/year level ($ST_{0.01}$). Time series of qn-SSJPM-derived annual $ST_{0.01}$ values (black line) with a least squares best-fit harmonic function that represents the region's dominant tidal forcings (gray curve), which includes an 18.6-year period, a 4.4-year period, and a linear trend. Legends show the ranges (i.e. double the amplitude) of the best-fit sinusoids and the slopes of the linear trends. Note the gap in the Eastport $ST_{0.01}$ time series where winter seasons were omitted due to less than 75% data completeness (see Tab. 1).

Figure 6. Joint impact of tidal forcing and sea-level rise on future flood hazard increase. *(Top panel)* 18.6 and 4.4-year components of the best-fit harmonic function to the winter $ST_{0.01}$ time series from Fig. 5. *(Bottom panel)* Gray curves show projected rates of local RCP8.5 SLR modified from Kopp et al. (2014) (line = 50^{th} quantile of samples, shading = central 90% range). Over 9.3-year-intervals where the nodal cycle is moving from a minimum to a maximum (indicated by red shading), the average nodal forcing rate (black triangle on y-axis) is added to the average projected rate of SLR over the same 9.3 years (red circles, with bars representing SLR uncertainty). Over intervals when the nodal cycle is trending negatively, nodal forcing is subtracted from the rate of SLR (blue circles and bars). The historical rate of SLR over the past century is also shown for reference (black asterisk on the y-axis).

References

Arns, A., Wahl, T., Haigh, I. D., Jensen, J., & Pattiaratchi, C. (2013). Estimating extreme water level probabilities: A comparison of the direct methods and recommendations for best practise. *Coastal Engineering*, *81*, 51–66. https://doi.org/10.1016/j.coastaleng.2013.07.003

Batstone, C., Lawless, M., Tawn, J., Horsburgh, K., Blackman, D., McMillan, A., Worth, D., Laeger, S., & Hunt, T. (2013). A UK best-practice approach for extreme sea-level analysis along complex topographic coastlines. *Ocean Engineering*, *71*, 28–39. https://doi.org/10.1016/j.oceaneng.2013.02.003

Bertin, X., de Bakker, A., van Dongeren, A., Coco, G., André, G., Ardhuin, F., et al. (2018). Infragravity waves: From driving mechanisms to impacts. *Earth-Science Reviews, 177*, 774–799. https://doi.org/10.1016/j.earscirev.2018.01.002

Buchanan, M. K., Kopp, R. E., Oppenheimer, M., & Tebaldi, C. (2016). Allowances for evolving coastal flood risk under uncertain local sea-level rise. *Climatic Change*, *137*(3), 347–362. https://doi.org/10.1007/s10584-016-1664-7

Buchanan, M. K., Oppenheimer, M., & Kopp, R. E. (2017). Amplification of flood frequencies with local sea level rise and emerging flood regimes. *Environmental Research Letters*, *12*(6), 064009. https://doi.org/10.1088/1748-9326/aa6cb3

Caldwell, P. C., Merrifield, M. A., & Thompson, P. R. (2010). *Sea level measured by tide gauges from global oceans as part of the Joint Archive for Sea Level (JASL) since 1846* [Data set]. National Oceanographic Data Center, NOAA. https://doi.org/10.7289/V5V40S7W

Church, J. A., Clark, P. U., Cazenave, A., Gregory, J. M., Jevrejeva, S., Levermann, A., Merrifield, M. A., Milne, G. A., Nerem, R. S., Nunn, P. D., Payne, A. J., Pfeffer, W. T., Stammer, D., & Unnikrishnan, A. S. (2013). *Sea level change* [Technical Report]. P.M.Cambridge University Press. http://drs.nio.org/drs/handle/2264/4605

Coles, S. (2001). *An Introduction to Statistical Modeling of Extreme Values*. Springer.

Dodet, G., Melet, A., Ardhuin, F., Bertin, X., Idier, D., & Almar, R. (2019). The Contribution of Wind-Generated Waves to Coastal Sea-Level Changes. *Surveys in Geophysics, 40(6)*, 1563–1601. https://doi.org/10.1007/s10712-019-09557-5

Douglas, E., Kirshen, P., DeConto, R. M., FitzGerald, D. M., Hay, C., Hughes, Z., Kemp, A. C., Kopp, R. E., Anderson, B., Kuang, Z., Ravela, S., Woodruff, J. D., Barlow, M., Collins, M., DeGaetano, A., Schlosser, C. A., Ganguly, A., Kodra, E., & Ruth, M. (2016). *Climate change and sea level rise projections for Boston: The Boston Research Advisory Group report.* (p. 54). Climate Ready Boston. https://www.boston.gov/sites/default/files/document-file-12-2016/brag_report_-_final.pdf

Eliot, M. (2010). Influence of interannual tidal modulation on coastal flooding along the Western Australian coast. *Journal of Geophysical Research: Oceans*, *115*(C11). https://doi.org/10.1029/2010JC006306

683 Emanuel, K. A. (2013). Downscaling CMIP5 climate models shows increased tropical cyclone
684 activity over the 21st century. *Proceedings of the National Academy of Sciences*, *110*(30),
685 12219–12224. https://doi.org/10.1073/pnas.1301293110

686 Familkhalili, R., Talke, S. A., & Jay, D. A. (n.d.). Tide-Storm Surge Interactions in Highly
687 Altered Estuaries: How Channel Deepening Increases Surge Vulnerability. *Journal of*
688 *Geophysical Research: Oceans*, *n/a*(n/a), e2019JC015286.
689 https://doi.org/10.1029/2019JC015286

690 Ferro, C. A. T., & Segers, J. (2003). Inference for clusters of extreme values. *Journal of the*
691 *Royal Statistical Society: Series B (Statistical Methodology)*, *65*(2), 545–556.
692 https://doi.org/10.1111/1467-9868.00401

693 Galloway, G. E., Baecher, G. B., Plasencia, D., Coulton, K. G., Louthain, J., Bagha, M., & Levy,
694 A. R. (2006). *Assessing the Adequacy of the National Flood Insurance Program's 1 Percent*
695 *Flood Standard* (p. 197) [2001-2006 Evalulation of the National Flood Insurance Program].
696 http://s3-us-gov-west-1.amazonaws.com/dam-production/uploads/20130726-1602-20490-
697 6095/nfip_eval_1_percent_standard.pdf

698 Garner, A. J., Mann, M. E., Emanuel, K. A., Kopp, R. E., Lin, N., Alley, R. B., Horton, B. J.,
699 DeConto, R. M., Donnelly, J. P., & Pollard, D. (2017). Impact of climate change on New
700 York City's coastal flood hazard: Increasing flood heights from the preindustrial to 2300
701 CE. *Proceedings of the National Academy of Sciences*, *114*(45), 11861–11866.
702 https://doi.org/10.1073/pnas.1703568114

703 Garrett, C. (1972). Tidal Resonance in the Bay of Fundy and Gulf of Maine. *Nature*, *238*(5365),
704 441–443. https://doi.org/10.1038/238441a0

705 Goddard, P. B., Yin, J., Griffies, S. M., & Zhang, S. (2015). An extreme event of sea-level rise
706 along the Northeast coast of North America in 2009–2010. *Nature Communications*, *6*(1),
707 1–9. https://doi.org/10.1038/ncomms7346

708 Godin, G. (1993). On tidal resonance. *Continental Shelf Research*, *13*(1), 89–107.
709 https://doi.org/10.1016/0278-4343(93)90037-X

710 Greenberg, D. A., Blanchard, W., Smith, B., & Barrow, E. (2012). Climate Change, Mean Sea
711 Level and High Tides in the Bay of Fundy. *Atmosphere-Ocean*, *50*(3), 261–276.
712 https://doi.org/10.1080/07055900.2012.668670

713 Griggs, G., Arvai, J., Cayan, D., DeConto, R. M., Fox, J., Fricker, H. A., Kopp, R. E., Tebaldi,
714 C., & Whiteman, E. A. (2017). *Rising seas in California: An update on sea-level rise*
715 *science.* (p. 71) [California Ocean Science Trust Tech. Rep.].
716 http://climate.calcommons.org/bib/rising-seas-california-update-sea-level-rise-science

717 Haigh, I. D., Eliot, M., & Pattiaratchi, C. (2011). Global influences of the 18.61 year nodal cycle
718 and 8.85 year cycle of lunar perigee on high tidal levels. *Journal of Geophysical Research:*
719 *Oceans*, *116*(C6). https://doi.org/10.1029/2010JC006645

Haigh, I. D., Nicholls, R., & Wells, N. (2010). A comparison of the main methods for estimating probabilities of extreme still water levels. *Coastal Engineering*, *57*(9), 838–849. https://doi.org/10.1016/j.coastaleng.2010.04.002

Haigh, I. D., Pickering, M. D., Green, J. A. M., Arbic, B. K., Arns, A., Dangendorf, S., Hill, D. F., Horsburgh, K., Howard, T., Idier, D., Jay, D. A., Jänicke, L., Lee, S. B., Müller, M., Schindelegger, M., Talke, S. A., Wilmes, S.-B., & Woodworth, P. L. (2020). The Tides They Are A-Changin': A Comprehensive Review of Past and Future Nonastronomical Changes in Tides, Their Driving Mechanisms, and Future Implications. *Reviews of Geophysics*, *58*(1), e2018RG000636. https://doi.org/10.1029/2018RG000636

Hallegatte, S., Green, C., Nicholls, R. J., & Corfee-Morlot, J. (2013). Future flood losses in major coastal cities. *Nature Climate Change*, *3*(9), 802–806. https://doi.org/10.1038/nclimate1979

Horsburgh, K. J., Williams, J. A., Flowerdew, J., & Mylne, K. (2008). Aspects of operational forecast model skill during an extreme storm surge event. *Journal of Flood Risk Management*, *1*(4), 213–221. https://doi.org/10.1111/j.1753-318X.2008.00020.x

Hunter, J. (2010). Estimating sea-level extremes under conditions of uncertain sea-level rise. *Climatic Change*, *99*(3), 331–350. https://doi.org/10.1007/s10584-009-9671-6

Kendall, M. G. (1938). A New Measure of Rank Correlation. *Biometrika*, *30*(1/2), 81–93. JSTOR. https://doi.org/10.2307/2332226

Kirshen, P., Knee, K., & Ruth, M. (2008). Climate change and coastal flooding in Metro Boston: Impacts and adaptation strategies. *Climatic Change*, *90*(4), 453–473. https://doi.org/10.1007/s10584-008-9398-9

Knutson, T. R., McBride, J. L., Chan, J., Emanuel, K., Holland, G., Landsea, C., Held, I., Kossin, J. P., Srivastava, A. K., & Sugi, M. (2010). Tropical cyclones and climate change. *Nature Geoscience*, *3*(3), 157–163. https://doi.org/10.1038/ngeo779

Kopp, R. E., Horton, R. M., Little, C. M., Mitrovica, J. X., Oppenheimer, M., Rasmussen, D. J., Strauss, B. H., & Tebaldi, C. (2014). Probabilistic 21st and 22nd century sea-level projections at a global network of tide-gauge sites. *Earth's Future*, *2*(8), 383–406. https://doi.org/10.1002/2014EF000239

Ku, L.-F., Greenberg, D. A., Garrett, C. J. R., & Dobson, F. W. (1985). Nodal Modulation of the Lunar Semidiurnal Tide in the Bay of Fundy and Gulf of Maine. *Science*, *230*(4721), 69–71. https://doi.org/10.1126/science.230.4721.69

Lambert, E., Rohmer, J., Cozannet, G. L., & Wal, R. S. W. van de. (2020). Adaptation time to magnified flood hazards underestimated when derived from tide gauge records. *Environmental Research Letters*. https://doi.org/10.1088/1748-9326/ab8336

Leadbetter, M. R. (1983). Extremes and local dependence in stationary sequences. *Zeitschrift Für Wahrscheinlichkeitstheorie Und Verwandte Gebiete*, *65*(2), 291–306. https://doi.org/10.1007/BF00532484

Leffler, K., & Jay, D. A. (2009). Enhancing tidal harmonic analysis: Robust (hybrid L1/L2) solutions. *Continental Shelf Research*, *29*(1), 78–88. https://doi.org/10.1016/j.csr.2008.04.011

Lin, N., Emanuel, K. A., Smith, J. A., & Vanmarcke, E. (2010). Risk assessment of hurricane storm surge for New York City. *Journal of Geophysical Research: Atmospheres*, *115*(D18). https://doi.org/10.1029/2009JD013630

Melet, A., Meyssignac, B., Almar, R., & Le Cozannet, G. (2018). Under-estimated wave contribution to coastal sea-level rise. *Nature Climate Change, 8(3),* 234–239. https://doi.org/10.1038/s41558-018-0088-y

Menéndez, M., & Woodworth, P. L. (2010). Changes in extreme high water levels based on a quasi-global tide-gauge data set. *Journal of Geophysical Research: Oceans*, *115*(C10). https://doi.org/10.1029/2009JC005997

Müller, M., Arbic, B. K., & Mitrovica, J. X. (2011). Secular trends in ocean tides: Observations and model results. *Journal of Geophysical Research: Oceans, 116(C5)*. https://doi.org/10.1029/2010JC006387

Müller, M. (2012). The influence of changing stratification conditions on barotropic tidal transport and its implications for seasonal and secular changes of tides. *Continental Shelf Research*, *47*, 107–118. https://doi.org/10.1016/j.csr.2012.07.003

National Environment Research Council (1975). *The Flood Studies Report*. London: Natural Environment Research Council.

Neumann, B., Vafeidis, A. T., Zimmermann, J., & Nicholls, R. J. (2015). Future Coastal Population Growth and Exposure to Sea-Level Rise and Coastal Flooding—A Global Assessment. *PLOS ONE*, *10*(3), e0118571. https://doi.org/10.1371/journal.pone.0118571

NYC. (2013). *A stronger, more resilient New York* (p. 435) [New York City PlaNYC Tech Rep.]. https://www1.nyc.gov/assets/sirr/downloads/pdf/Ch_2_ClimateAnalysis_FINAL_singles.pdf

Oppenheimer, M., Glavovic, B. C., Hinkel, J., van de Wal, R., Magnan, A. K., Abd-Elgawad, A., Cai, R., Cifuentes-Jara, M., DeConto, R. M., Ghosh, T., Hay, J., Isla, F., Marzeion, B., Meyssignac, B., & Sebesvari, Z. (n.d.). *Sea Level Rise and Implications for Low-Lying Islands, Coasts and Communities.* (IPCC Special Report on the Ocean and Cryosphere in a Changing Climate).

Pawlowicz, R., Beardsley, B., & Lentz, S. (2002). Classical tidal harmonic analysis including error estimates in MATLAB using T_TIDE. *Computers & Geosciences*, *28*(8), 929–937. https://doi.org/10.1016/S0098-3004(02)00013-4

Pelling, H. E., & Green, J. A. M. (2013). Sea level rise and tidal power plants in the Gulf of Maine. *Journal of Geophysical Research: Oceans*, *118*(6), 2863–2873. https://doi.org/10.1002/jgrc.20221

Peng, D., Hill, E. M., Meltzner, A. J., & Switzer, A. D. (2019). Tide Gauge Records Show That the 18.61-Year Nodal Tidal Cycle Can Change High Water Levels by up to 30 cm. *Journal of Geophysical Research: Oceans*, *124*(1), 736–749. https://doi.org/10.1029/2018JC014695

Pugh D. T., & Vassie J. M. (1978). Extreme Sea Levels from Tide and Surge Probability. *Coastal Engineering 1978*, 911–930. https://doi.org/10.1061/9780872621909.054

Pugh, D., & Vassie, J. (1980). Applications of the joint probability method for extreme sea level computations. *Proceedings of the Institution of Civil Engineers*, *69*(4), 959–975. https://doi.org/10.1680/iicep.1980.2179

Rabinovich, A. B. (2009). Seiches and Harbor Oscillations. *In: Handbook of Coastal and Ocean Engineering* (Vol. 1–0, pp. 193–236). WORLD SCIENTIFIC. https://doi.org/10.1142/9789812819307_0009

Ray, R. D. (2006). Secular changes of the M2 tide in the Gulf of Maine. *Continental Shelf Research*, *26*(3), 422–427. https://doi.org/10.1016/j.csr.2005.12.005

Ray, R. D., & Merrifield, M. A. (2019). The Semiannual and 4.4-Year Modulations of Extreme High Tides. *Journal of Geophysical Research: Oceans*, *124*(8), 5907–5922. https://doi.org/10.1029/2019JC015061

Ray, R. D., & Talke, S. A. (2019). Nineteenth-Century Tides in the Gulf of Maine and Implications for Secular Trends. *Journal of Geophysical Research: Oceans*, *124*(10), 7046–7067. https://doi.org/10.1029/2019JC015277

Ray, Richard D., & Foster, G. (2016). Future nuisance flooding at Boston caused by astronomical tides alone. *Earth's Future*, *4*(12), 578–587. https://doi.org/10.1002/2016EF000423

Schindelegger, M., Green, J. a. M., Wilmes, S.-B., & Haigh, I. D. (2018). Can We Model the Effect of Observed Sea Level Rise on Tides? *Journal of Geophysical Research: Oceans*, *123*(7), 4593–4609. https://doi.org/10.1029/2018JC013959

Sobey, R. J. (2005). Extreme low and high water levels. *Coastal Engineering, 52(1)*, 63–77. https://doi.org/10.1016/j.coastaleng.2004.09.003

Talke, S. A., Kemp, A. C., & Woodruff, J. (2018). Relative Sea Level, Tides, and Extreme Water Levels in Boston Harbor From 1825 to 2018. *Journal of Geophysical Research: Oceans*, *123*(6), 3895–3914. https://doi.org/10.1029/2017JC013645

826 Talke, S. A., Mahedy, A., Jay, D. A., Lau, P., Hilley, C., & Hudson, A. (2020). Sea Level, Tidal,
827 and River Flow Trends in the Lower Columbia River Estuary, 1853–present. *Journal of*
828 *Geophysical Research: Oceans*, *125*(3), e2019JC015656.
829 https://doi.org/10.1029/2019JC015656

830 Talke, Stefan A, & Jay, D. A. (2020). Changing Tides: The Role of Natural and Anthropogenic
831 Factors. *Annual Review of Marine Science*, *12*, 121–151. https://doi.org/10.1146/annurev-
832 marine-010419-010727

833 Tawn, J. A., & Vassie, J. M. (1989). *Extreme Sea Levels: the Joint Probabilities Method*
834 *Revisited and Revised*. https://trid.trb.org/view/435293

835 Tawn, Jonathan A. (1992). Estimating Probabilities of Extreme Sea-Levels. *Journal of the Royal*
836 *Statistical Society: Series C (Applied Statistics)*, *41*(1), 77–93.
837 https://doi.org/10.2307/2347619

838 Tebaldi, C., Strauss, B. H., & Zervas, C. E. (2012). Modelling sea level rise impacts on storm
839 surges along US coasts. *Environmental Research Letters*, *7*(1), 014032.
840 https://doi.org/10.1088/1748-9326/7/1/014032

841 Thompson, P. R., Mitchum, G. T., Vonesch, C., & Li, J. (2013). Variability of Winter
842 Storminess in the Eastern United States during the Twentieth Century from Tide Gauges.
843 *Journal of Climate*, *26*(23), 9713–9726. https://doi.org/10.1175/JCLI-D-12-00561.1

844 Vousdoukas, M. I., Voukouvalas, E., Mentaschi, L., Dottori, F., Giardino, A., Bouziotas, D.,
845 Bianchi, A., Salamon, P., & Feyen, L. (2016). Developments in large-scale coastal flood
846 hazard mapping. *Natural Hazards and Earth System Sciences*, *16*(8), 1841–1853.
847 https://doi.org/10.5194/nhess-16-1841-2016

848 Wahl, T., Haigh, I. D., Nicholls, R. J., Arns, A., Dangendorf, S., Hinkel, J., & Slangen, A. B. A.
849 (2017). Understanding extreme sea levels for broad-scale coastal impact and adaptation
850 analysis. *Nature Communications*, *8*(1), 1–12. https://doi.org/10.1038/ncomms16075

851 Wahl, Thomas, & Chambers, D. P. (2015). Evidence for multidecadal variability in US extreme
852 sea level records. *Journal of Geophysical Research: Oceans*, *120*(3), 1527–1544.
853 https://doi.org/10.1002/2014JC010443

854 Williams, J., Horsburgh, K. J., Williams, J. A., & Proctor, R. N. F. (2016). Tide and skew surge
855 independence: New insights for flood risk. *Geophysical Research Letters*, *43*(12), 6410–
856 6417. https://doi.org/10.1002/2016GL069522

857 Winterwerp, J. C., Wang, Z. B., van Braeckel, A., van Holland, G., & Kösters, F. (2013). Man-
858 induced regime shifts in small estuaries—II: A comparison of rivers. *Ocean Dynamics*,
859 *63*(11), 1293–1306. https://doi.org/10.1007/s10236-013-0663-8

860 Woodworth, P. L. (2010). A survey of recent changes in the main components of the ocean tide.
861 *Continental Shelf Research*, *30*(15), 1680–1691. https://doi.org/10.1016/j.csr.2010.07.002

Woodworth, P. L., Melet, A., Marcos, M., Ray, R. D., Wöppelmann, G., Sasaki, Y. N., Cirano, M., Hibbert, A., Huthnance, J. M., Monserrat, S., & Merrifield, M. A. (2019). Forcing Factors Affecting Sea Level Changes at the Coast. *Surveys in Geophysics, 40(6)*, 1351–1397. https://doi.org/10.1007/s10712-019-09531-1

Zervas, C. (2013). *Extreme Water Levels of the United States 1893-2010* (NOAA Technical Report NOS CO-OPS 067; p. 200). NOAA. https://tidesandcurrents.noaa.gov/publications/NOAA_Technical_Report_NOS_COOPS_067a.pdf

Figure 1.

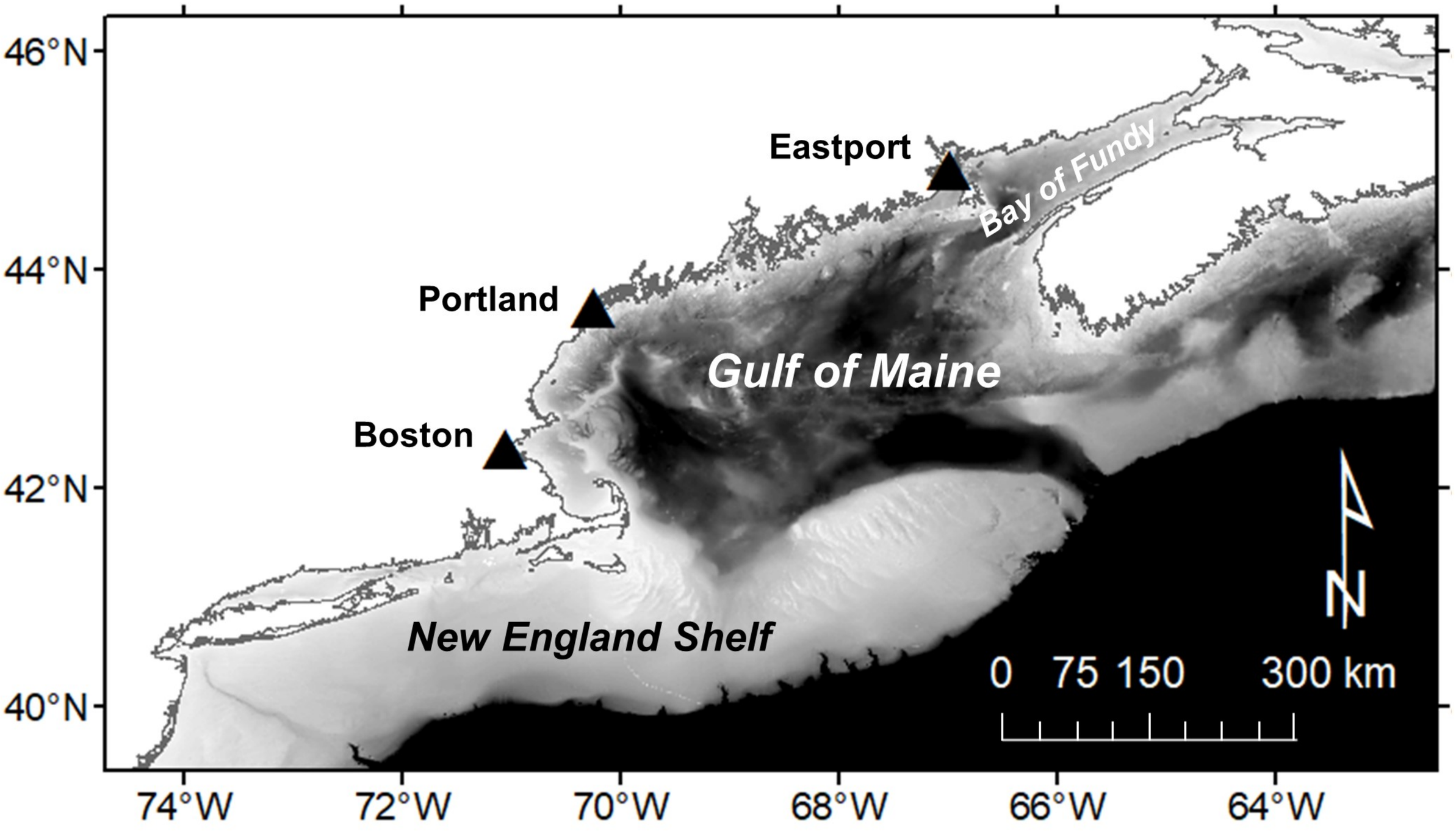
46°N
44°N
42°N
40°N
74°W
72°W
70°W
68°W
66°W
64°W
Eastport
Bay of Fundy
Portland
Gulf of Maine
Boston
New England Shelf
N
0 75 150 300 km

Figure 2.

a

b

Full-year

Summer

Winter

qn-SSJPM

GPD_{ST}

Empirical

Eastport
MHHW 2.92 m

Eastport

Portland
MHHW 1.51 m

Portland

Boston
MHHW 1.55 m

Boston

Expected exceedances/year

1
0.1
0.01

4
4.5
5

2.5
3
3.5

Storm Tide (m above annual MSL)

Figure 3.

qn-SSJPM

GPD_{ST}

a

% trials containing truth in central 67% range

67%

60

40

20

0

0.1

0.01

0.002

b

0.8

✳ = mean

0.4

0

-0.4

Estimate bias (m)

0.1

0.01

0.002

Expected exceedances/year

Figure 4.

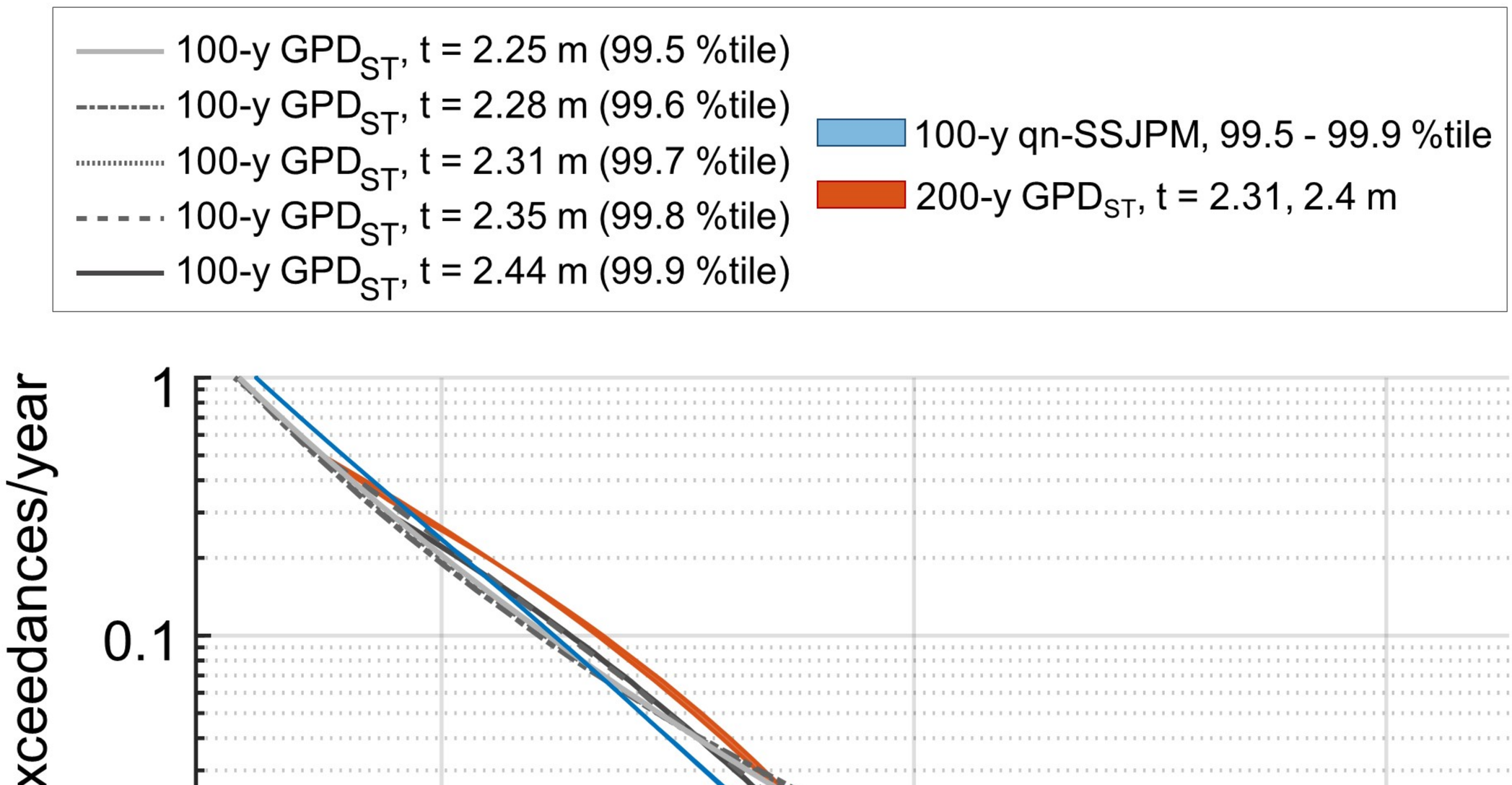
100-y GPD$_{ST}$, t = 2.25 m (99.5 %tile)
100-y GPD$_{ST}$, t = 2.28 m (99.6 %tile)
100-y GPD$_{ST}$, t = 2.31 m (99.7 %tile)
100-y GPD$_{ST}$, t = 2.35 m (99.8 %tile)
100-y GPD$_{ST}$, t = 2.44 m (99.9 %tile)
100-y qn-SSJPM, 99.5 - 99.9 %tile
200-y GPD$_{ST}$, t = 2.31, 2.4 m
Expected exceedances/year
1
0.1
0.01
2.5
3
3.5
Storm Tide (m above annual MSL)

Figure 5.

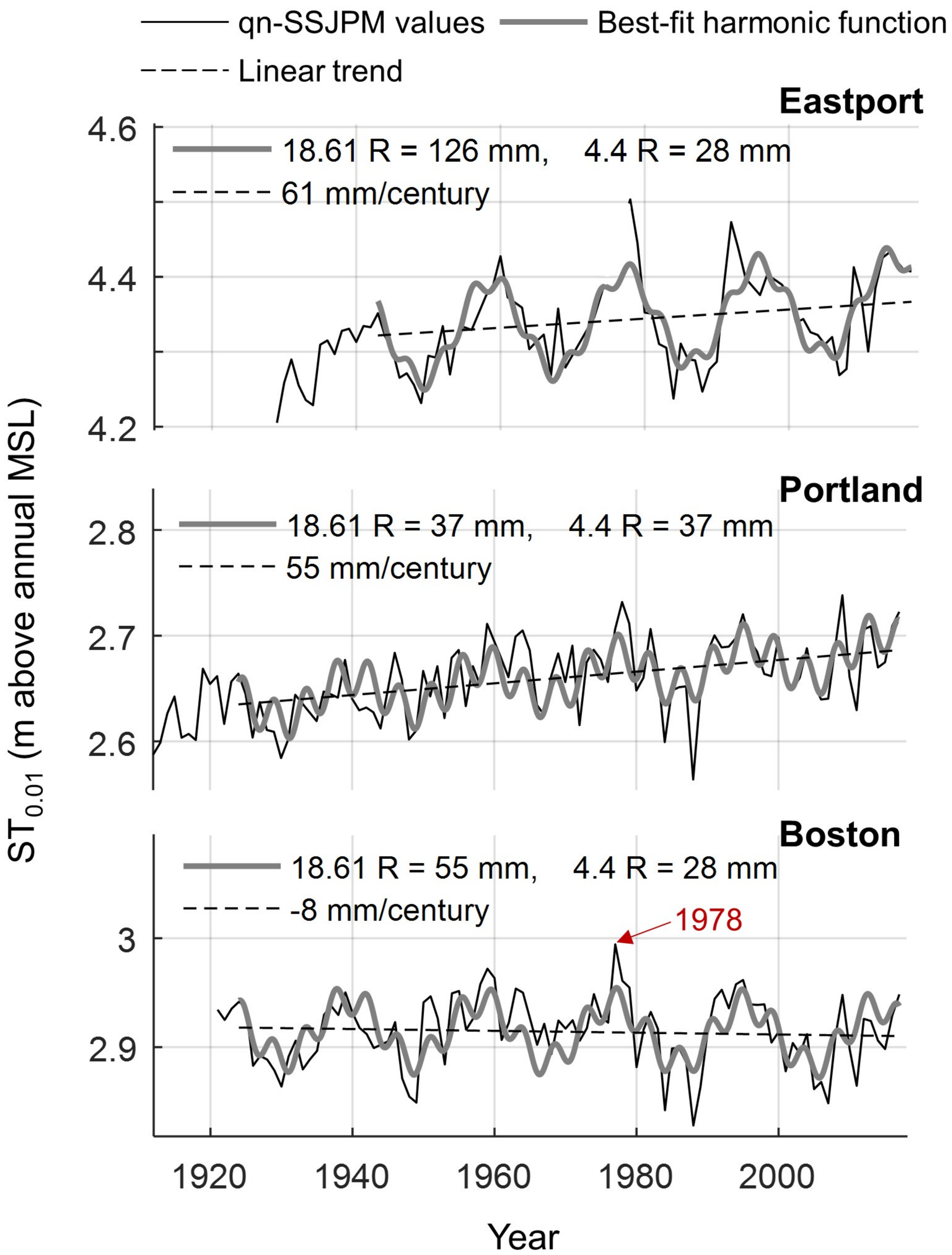
qn-SSJPM values
Best-fit harmonic function
Linear trend
Eastport
18.61 R = 126 mm, 4.4 R = 28 mm
61 mm/century
4.6
4.4
4.2
Portland
18.61 R = 37 mm, 4.4 R = 37 mm
55 mm/century
2.8
2.7
2.6
Boston
18.61 R = 55 mm, 4.4 R = 28 mm
-8 mm/century
1978
3
2.9
$ST_{0.01}$ (m above annual MSL)
1920
1940
1960
1980
2000
Year

Figure 6.

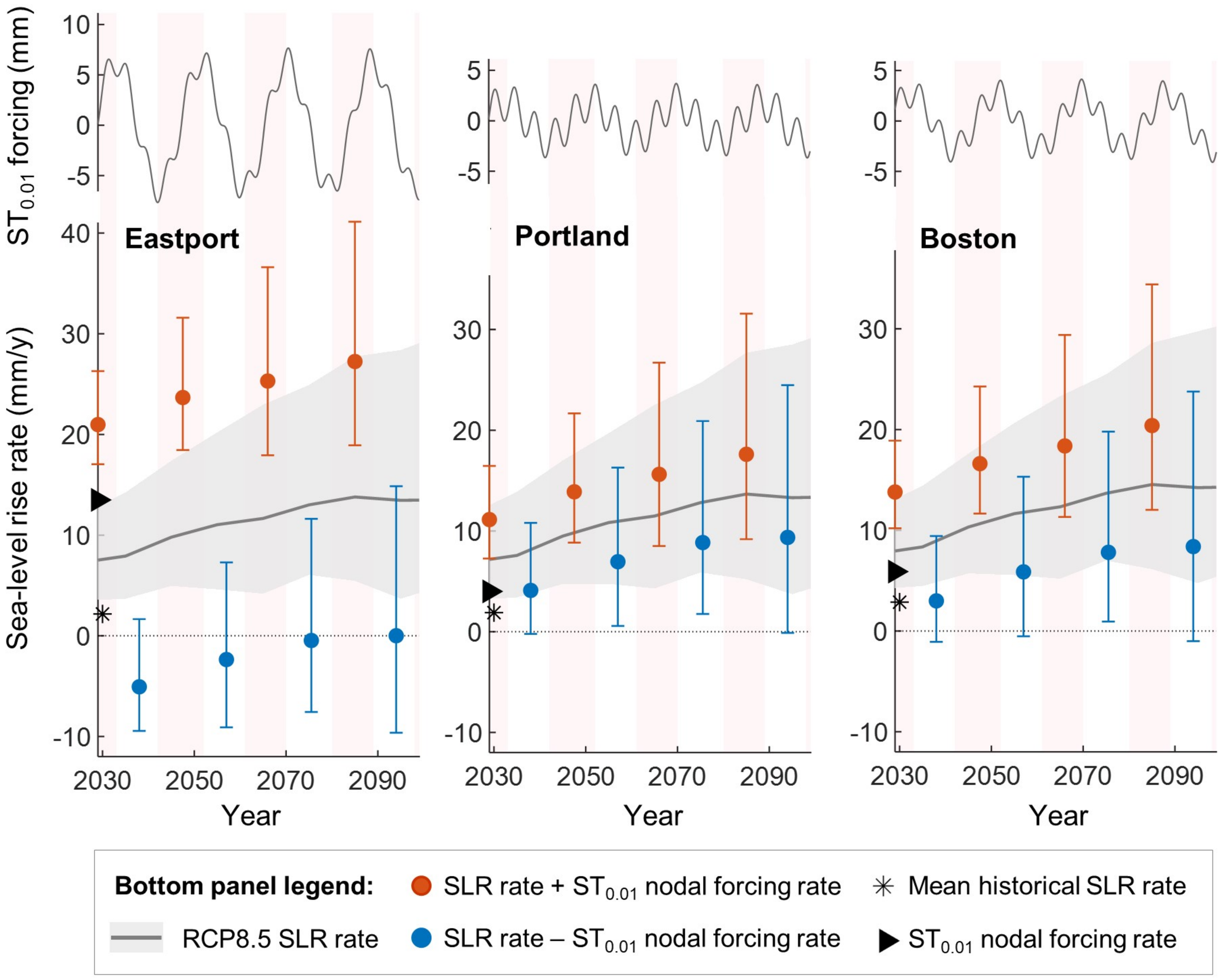
ST0.01 forcing (mm)
Sea-level rise rate (mm/y)
Eastport
Portland
Boston
Year
Bottom panel legend:
SLR rate + ST0.01 nodal forcing rate
SLR rate – ST0.01 nodal forcing rate
RCP8.5 SLR rate
Mean historical SLR rate
ST0.01 nodal forcing rate